



# Experimental and Theoretical Investigation on the Thermo-Mechanical Properties of Recycled Aggregate Concrete Containing Recycled Rubber

Yunchao Tang<sup>1,2</sup>, Wanhui Feng<sup>2\*</sup>, Zheng Chen<sup>1\*</sup>, Yumei Nong<sup>1</sup>, Minhui Yao<sup>2</sup> and Junhui Liu<sup>2</sup>

<sup>1</sup>Key Laboratory of Disaster Prevention and Structural Safety of China Ministry of Education, School of Civil Engineering and Architecture, Guangxi University, Nanning, China, <sup>2</sup>College of Urban and Rural Construction, Zhongkai University of Agriculture and Engineering, Guangzhou, China

## OPEN ACCESS

### Edited by:

Fernando Fraternali,  
University of Salerno, Italy

### Reviewed by:

Enzo Martinelli,  
University of Salerno, Italy  
Antonio Caggiano,  
Darmstadt University of Technology,  
Germany

### \*Correspondence:

Wanhui Feng  
whfeng@zhku.edu.cn  
Zheng Chen  
chenzheng@gxu.edu.cn

### Specialty section:

This article was submitted to  
Mechanics of Materials,  
a section of the journal  
Frontiers in Materials

**Received:** 18 January 2021

**Accepted:** 15 February 2021

**Published:** 05 April 2021

### Citation:

Tang Y, Feng W, Chen Z, Nong Y,  
Yao M and Liu J (2021) Experimental  
and Theoretical Investigation on the  
Thermo-Mechanical Properties of  
Recycled Aggregate Concrete  
Containing Recycled Rubber.  
Front. Mater. 8:655097.  
doi: 10.3389/fmats.2021.655097

The utilization of recycled aggregates made from construction wastes and recycled rubber made from waste tires is an effective method to realize the sustainable development. Thus, this study aims to determine the feasibility of using recycled aggregate concrete containing rubber, named rubberized recycled aggregate concrete (RRAC) as a new type of green-building material. The experimental carbon emissions test verified RRAC as a low-carbon material. In addition, the residual mechanical properties of RRAC were investigated under elevated temperatures. After exposure at 200, 400, and 600 C for 60 min, the stress–strain curve, compressive strength, energy absorption capacity, and spalling resistance of RRAC with recycled aggregate replacement ratios of 50 and 100%, rubber contents of 0, 5, 10, and 15% were explored with microstructural analysis. Moreover, empirical models were proposed to describe the effects of heated temperatures and rubber contents on the stress–strain relationship of RRAC. The results indicated that the rubber particles could reduce the spalling of specimens based on the vapor pressure theory. Therefore, this study provided scientific guidance for the design of structures made with RRAC for resisting high temperatures.

**Keywords:** recycled aggregate concrete containing rubber 1, high-temperature treatment 2, residual compressive properties 3, constitutive model 4, microstructural analysis 5, carbon emission 6

## INTRODUCTION

In recent years, an enormous number of buildings, pavements, and bridges have expired out of service life with the improvement of urbanization, causing the amount of waste concrete to increase rapidly. Consequently, the construction industry has been committed to the development of sustainable resources, focusing on innovations and using recycled materials for limited natural aggregates. The common construction waste is mainly waste concrete and masonry materials that can be converted into recycled aggregates (RAs) with a particular program treatment and can be utilized to replace some of natural aggregates (NAs) to produce recycled aggregate concrete (RAC) (Tang et al., 2018; Xiao et al., 2018; Tang et al., 2019; Tang et al., 2020; Xiong et al., 2020). The use of RA can not only alleviate the current situation of natural resources (Ahmed and Lim, 2021) but also

reduce environmental pollution, CO<sub>2</sub> emissions, and land occupation resulting from a large amount of construction waste (Arulrajah et al., 2015).

Most studies on RAC have focused on the mechanical properties at ambient temperature. As the surfaces of RAs are covered with old mortar, the interfacial transition zones (ITZs) in RAC are significantly influenced. Compared to natural aggregate concrete (NAC), RAC has a higher void ratio (Xiao et al., 2018; Pradhan et al., 2020) and more number of internal microcracks (Koenders et al., 2014), causing its mechanical properties to be dramatically different. Therefore, strict design procedures are needed to control the structural production procedure of the RAC (Choi and Yun, 2012). Moreover, many concrete structures are easily damaged by fire during their service life, and the fire performance of the structure must be considered in relevant codes (ACI 216.1, 2007). Therefore, the fire performance of RAC should be further studied to promote its use. Previous research (Khoury, 2000; Sarhat and Sherwood, 2013) states that the difference in thermal expansion properties between the aggregates and mortar is vital for decreasing thermo-damage; the thermal expansion coefficient of RA is close to that of mortar and lower than that of NA. This statement has been verified by certain studies as well (Xiao et al., 2013; Meng et al., 2017; Xuan et al., 2017). Furthermore, Xuan et al. (2017) pointed out that RA can enhance the thermal properties of concrete. Xiao et al. (2013) also indicated that RAs have beneficial effects on the fire performance of concrete, especially with a large RA replacement ratio (more than 50%). Similarly, Meng et al. (2017) indicated that RAC with a large RA replacement ratio could enhance the fire performance of the concrete, and the optimal replacement ratio is 70%.

Besides, the rapid development of the automobile market is increasing the demand for rubber tires, which leads to an increasing amount of waste rubber. Based on the report from European Tyre and Rubber Manufacturer's Association, 3.6 billion kilograms of waste rubber was produced in Europe in 2013 (Asaro et al., 2018). The effective utilization of waste rubber is also an urgent problem. Scholars (Gupta et al., 2014; Feng et al., 2018, 2019; Feng et al., 2021; Xie et al., 2019) found that rubber particles (RPs) made with waste tires can enhance the crack resistance and deformation capacity of concrete, namely, rubberized concrete. In addition, the toughness (Reda Taha et al., 2008) and service life of rubberized concrete (Graeff et al., 2012; Liu et al., 2013) are better than those of ordinary concrete. However, the influence of rubberized concrete on the fire performance of the concrete is relevant for consideration because the properties of the concrete are significantly weakened at high temperatures. Based on the vapor pressure theory (Choe et al., 2019), RPs soften and decompose at high temperature, which leads to an increasing number of pores in the concrete and decreases the internal steam pressure. Thus, the improvement in fire performance of the concrete using RPs has been verified by several scholars (Li et al., 2011; Mousa, 2017). Therefore, the RPs can also be incorporated into the RAC to form rubberized recycled aggregate concrete (RRAC). In addition to being made of green recyclable materials, the

**TABLE 1** | Mix proportion and slump of RNAC and RRAC.

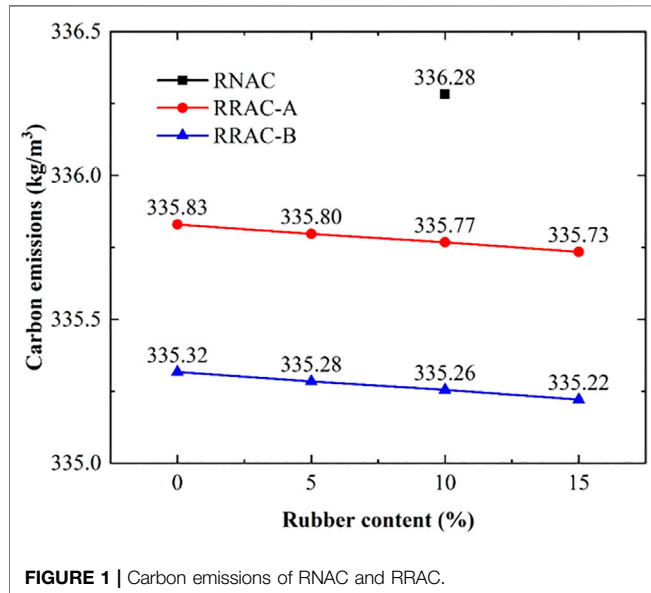
	Mix proportion (kg/m <sup>3</sup> )							Slump (mm)
	Water	Cement	RA	NA	Sand	RP	Water reducer	
RNAC-5	216	485	0	1,194	481	21	3.88	180
RAC-A	216	485	554	597	536	0	3.88	175
RRAC-A-5	216	485	554	597	507	11	3.88	165
RRAC-A-10	216	485	554	597	481	21	3.88	160
RRAC-A-15	216	485	554	597	451	32	3.88	80
RAC-B	216	485	1,109	0	536	0	3.88	170
RRAC-B-5	216	485	1,109	0	507	11	3.88	145
RRAC-B-10	216	485	1,109	0	481	21	3.88	125
RRAC-B-15	216	485	1,109	0	451	32	3.88	75

mechanical properties of RRAC are also excellent. Liu et al. (2015) found that RPs could enhance the fatigue performance of RAC. Moreover, the deformation capacity of RRAC was better than that of RAC under static (Chen et al., 2020) or impact loads (Li et al., 2016). However, few studies have focused on the thermo-mechanical performance of RRAC. Ganjian et al. (2009) reported that the properties of concrete varied significantly with more than 5% rubber content, and the toughness of RAC can be speculated to increase before the rubber softens and starts to decompose. In addition, the rubber decomposes or escapes through more number of pores in the RAC than the NAC at higher temperatures, thus releasing the internal steam pressure that further improves the high-temperature performance of the RAC.

It can be inferred from the above-mentioned research that adding a certain amount of rubber particles can effectively reduce the burst phenomenon of RAC. At present, there were few studies on the thermal-mechanical properties of RRAC, which did not focus on the stress-strain responses and microstructures of RRAC after exposure to high temperatures (Saberian et al., 2019). The mechanical properties of RRAC after heating at high temperatures including the optimal rubber content are necessary to be evaluated to further promote the use of RRAC. Thus, the purposes of this paper are to determine the mechanical properties of RRAC under high temperatures. Specifically, to investigate the thermal response as well as the residual mechanical properties after the high-temperature treatment. In careful consideration, large RA replacement ratios of 50 and 100% were used. The specimens were prepared with varying rubber contents (0, 5, 10, and 15%) and treated at different temperatures (25, 200, 400, and 600°C). The residual compression strength, deformation performance, stress-strain relationship, energy absorption capacity, and spalling mechanism of RRAC have been discussed. Finally, to further promote crumb rubber and recycled aggregate in the construction sector.

**TABLE 2** | Cp of each type of raw materials for RRAC.

Raw materials	Cement (Luo et al., 2016)	NA (Luo et al., 2016)	RA (Luo et al., 2016)	Water (Jiang et al., 2014)	Superplasticizer (Jiang et al., 2014)	Sand (Luo et al., 2016)	RP (Gustavsson et al., 2010)
$C_p$	685.74 kg/t	4.00 kg/m <sup>3</sup>	2.60 kg/m <sup>3</sup>	0.91 kg/m <sup>3</sup>	28.49 kg/t	3.19 kg/m <sup>3</sup>	133.34 kg/t

**FIGURE 1** | Carbon emissions of RNAC and RRAC.

## EXPERIMENTAL ARRANGEMENTS

### Mix Design and Carbon Emissions

Ordinary Portland cement with a compression strength of 42.5 MPa (P.O. 42.5R) was used. Continuous graded medium sand with a particle size of 0–4.75 mm, fineness modulus of 2.53, and an apparent density of 2,722 kg/m<sup>3</sup> was used. In addition, coarse aggregates included NAs and RAs. The particle sizes of NAs and RAs were both 5–35 mm. RAs were mixed into the RAC by replacing equal volumes of NAs—three mix proportions constituting 0, 50, and 100% replacement of NA with RA. The apparent density and the crushing index of NA were 1,627 kg/m<sup>3</sup> and 11.6%, and that of RA were 1,511 kg/m<sup>3</sup> and 7.6%, respectively. Moreover, the rubber was mixed into the RAC as per 0, 5, 10, and 15% of the volume of sand. RPs were of 40-mesh size (approximately 0.425 mm) with an apparent density of 1,030 kg/m<sup>3</sup>. Besides, a type of superplasticizer of polycarboxylic acid was employed.

The mix proportion is summarized in **Table 1**, where concise representations are used to distinguish the mix proportions based on preparation composition. RNAC represents rubberized natural aggregate concrete; A and B represent 50 and 100% replacement ratio of RA, and 5, 10, and 15 represent the replacement percentage of RPs. The slump of all groups is also summarized in **Table 1**, where an increase in the RA replacement rate exhibited a significant loss in the fluidity of the concrete

**TABLE 3** | Arrangement of specimens.

	Size (mm)	Quantity	Temperature (°C)
RNAC-5	Φ150 × 300	3 × 4	25, 200, 400, 600
RAC-A	Φ150 × 300	3 × 4	25, 200, 400, 600
RRAC-A-5	Φ150 × 300	3 × 4	25, 200, 400, 600
RRAC-A-10	Φ150 × 300	3 × 4	25, 200, 400, 600
RRAC-A-15	Φ150 × 300	3 × 4	25, 200, 400, 600
RAC-B	Φ150 × 300	3 × 4	25, 200, 400, 600
RRAC-B-5	Φ150 × 300	3 × 4	25, 200, 400, 600
RRAC-B-10	Φ150 × 300	3 × 4	25, 200, 400, 600
RRAC-B-15	Φ150 × 300	3 × 4	25, 200, 400, 600

owing to the strong absorption capacity of RAs. In addition, the fluidity of recycled concrete decreased continuously as the rubber content increasing, because the addition of rubber reduced the cohesion of the fresh mixture (Albano et al., 2005).

### Comparisons of Carbon Emissions

Increasing attention has been paid to the greenhouse gas emissions caused by concrete-like materials over the development of construction industrialization. According to the existing calculation method (Li and Chen, 2017; Xie et al., 2018), the total amount of carbon dioxide released from production  $E_u$  can be expressed as:

$$E_u = m \times C_p \quad (1)$$

where  $C_p$  is the emission factor of raw materials—summarized in **Table 2**—referring to the results of numerous studies. The total carbon emissions of all groups are presented in **Figure 1**, which shows that the incorporation of RAs and RPs could effectually reduce carbon emissions to a certain extent. As the amount of sand reduced with the increasing rubber content, a slight decrease in emissions can be observed from **Figure 1**. Upon complete replacement of NAs with RAs, approximately 1 kg of carbon dioxide could be reduced in the process of producing 1 m<sup>3</sup> of concrete. Therefore, RRAC was a type of low-carbon building material compared to ordinary concrete.

### Specimen Preparation and Heating Treatment

All samples were removed from the molds after 24 h. Thereafter, the specimens were cured at a standard condition, where constant temperature of 20 ± 2°C and relative humidity of 95% for 28 days. The size, quantity, and heating temperature of all cylindrical specimens are summarized in **Table 3**. After heating at various temperatures, three temperatures of 200, 400, and 600°C were

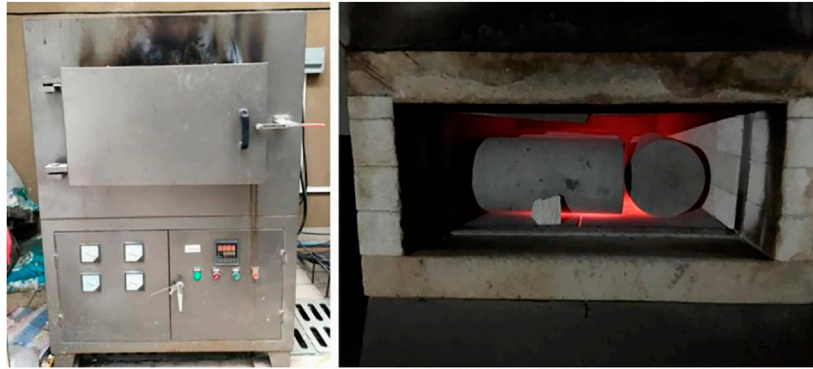


**FIGURE 2** | Photograph of the box type electric furnace.

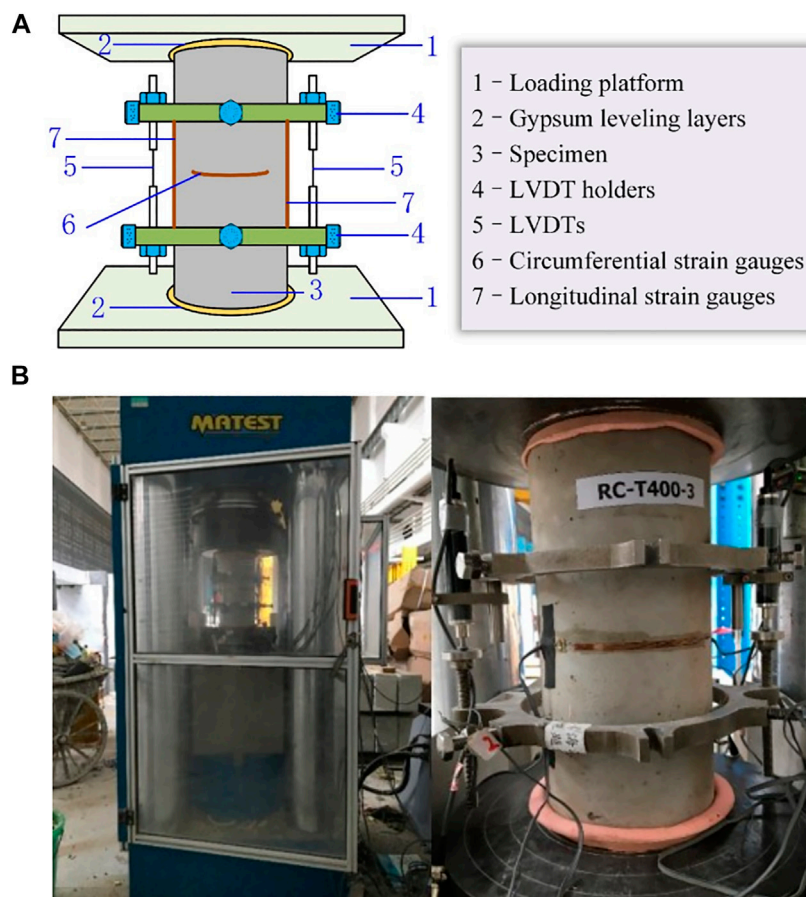


**FIGURE 3** | (A) Schematic diagram and (B) Test photo of the compression test.

selected apart from the ambient temperature (25°C) to investigate the compressive behaviors of RRAC.

### Heating Treatment

A box-type electric furnace (SX2-28-13, China) was used for the high-temperature treatment, as shown in **Figure 2**. The furnace

clearance size was 700 mm × 550 mm × 200 mm, rated power was 2 kW, maximum heating temperature was 1,000°C with a temperature controlling precision is ±1°C, and the heating element was a coarse-end type silicon-carbide rod. In addition, the distance between the specimen and the furnace wall is greater than 20 mm to ensure that the surface of the specimen was heated

**TABLE 4** | Experimental results of compression strength and elastic properties.

No	$f_c$ (MPa)				$E$ (GPa)				$\nu$			
	1	2	3	Avg	1	2	3	Avg	1	2	3	Avg
RNAC-5	53.55	53.62	55.98	54.38	31.46	29.74	30.30	30.50	0.20	0.19	0.21	0.20
RAC-A	57.99	54.80	58.75	57.18	32.80	32.48	30.34	31.87	0.18	0.20	0.18	0.19
RRAC-A-5	52.55	56.47	53.70	53.03	29.81	31.90	32.07	31.26	0.18	0.19	0.19	0.19
RRAC-A-10	–	52.37	52.22	52.30	–	30.00	29.95	29.60	–	0.16	0.18	0.18
RRAC-A-15	53.13	50.70	48.73	50.85	28.50	28.79	29.42	28.90	0.17	0.16	0.18	0.17
RAC-B	53.74	55.56	57.53	55.61	29.08	29.98	27.56	28.87	0.22	0.18	0.19	0.20
RRAC-B-5	52.07	–	53.74	52.91	28.36	–	27.45	27.91	0.19	–	0.21	0.20
RRAC-B-10	48.12	49.34	50.39	49.28	26.36	27.52	29.56	27.81	0.18	0.20	0.22	0.20
RRAC-B-15	46.75	41.90	45.69	44.78	27.61	26.58	24.94	26.38	0.21	0.21	0.19	0.20

Note: “–” represents the deviation from a reasonable range (15%).

evenly. The heating rate in this investigation was set to 5°C/min (Li et al., 2011). Upon reaching the target temperature, a constant temperature was maintained for 60 min, after which the heating was stopped; the specimens were taken out and naturally cooled at almost room temperature. The mass of each specimen was measured before and after heating. Thus, the mass loss of the RRAC was calculated and the color change and crack development in the specimens were observed.

### Compression Testing Method

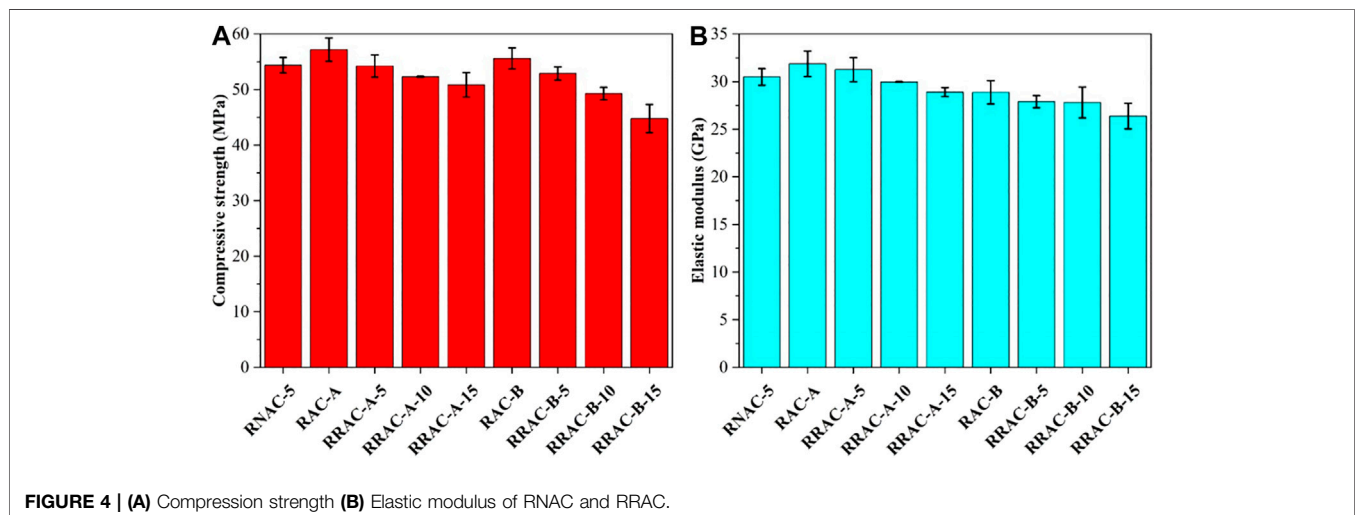
After heat treatments, as depicted in Figure 3, each flat surface of the cylinder were capped with a gypsum-leveling layer based on ASTM C617 (ASTM C617/C617M-15, 2015) before compression. Compression tests were carried out on a 4,000 kN universal testing machine (Matest C088-01, Italy). Based on the previous studies (Li et al., 2014; Guo et al., 2019), the loading rate on cylinders was uniformly constant to 0.18 mm/min. The longitudinal deformation of the cylinder was captured by using two linear variable differential transformers (LVDTs). Besides, two extra longitudinal strain gauges (BX120-10AA) were glued to corresponding positions of the specimen because of the low sensitivity of the LVDTs under small loads. Additionally, two more strain gauges (BX120-8AA) were utilized

to capture the circumferential strain of the cylinder during the test. Moreover, the synchronous displacement and force signals were recorded through a strain collection device (JM3841, Jing Ming Technology Co., Ltd, China), which has an acquisition frequency of 1 Hz. The specimens were pre-pressed with a small load before the formal test to ensure the uniform compression of the cylindrical surface and observe the strain signals of two longitudinal strain gauges. The compression test was started after confirmation, and the test was finished when the load exceeded 20% of the peak stress. After that, the uniaxial compressive response including the stress–strain relationship, Young’s modulus  $E$ , uniaxial compression strength  $f_c$  [ASTM C39 (ASTM C39/C39M-20, 2020)], and Poisson’s ratio  $\nu$  [ASTM C469 (ASTM C469/C469M-14, 2014)] could be obtained.

## EXPERIMENTAL RESULTS

### RRAC at Room Temperature

The effects of the recycled aggregate replacement ratio (0, 50, and 100%) and rubber particle content (0, 5, 10, and 15%) on the failure mode, stress–strain curve, compressive strength, modulus of elasticity, Poisson’s ratio, toughness, and specific toughness of

**FIGURE 4** | (A) Compression strength (B) Elastic modulus of RNAC and RRAC.

RRAC were analyzed at room temperature without heating treatment.

### Uniaxial Compression Strength and Elastic Properties

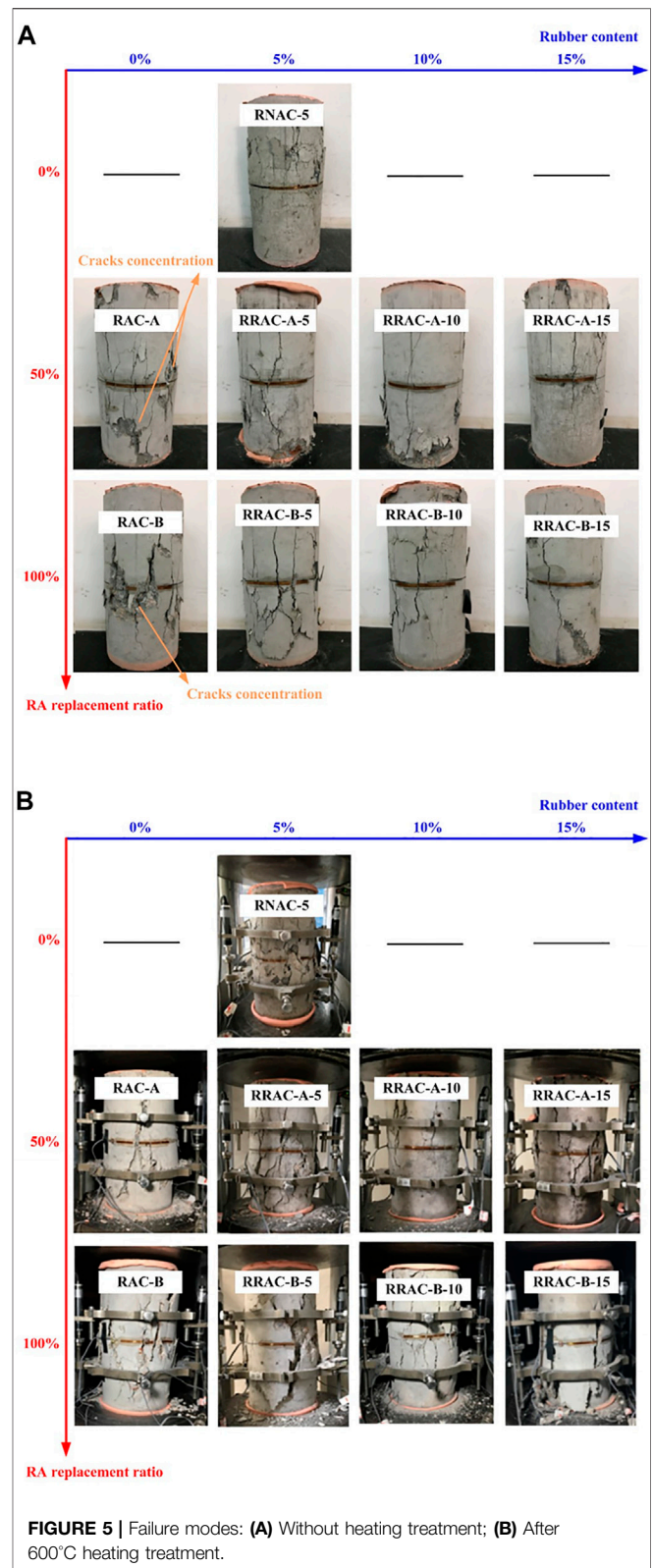
The experimental results of the compression strength and elastic properties, including Young's modulus and Poisson's ratio, are summarized in **Table 4**. As shown in **Figure 4A**, the compression strength of RRAC decreased slightly for specimens with higher RA replacement ratios. For instance, the compression strength was 3.82% lower than that of the natural aggregate concrete (RNAC-5) for a RA replacement ratio of 50% (RRAC-A-5). Similarly, the compressive strength for 100% RA replacement ratio (RRAC-B-5) was 9.38 and 5.77% lower than that of RNAC-5 and RRAC-A-5, respectively. Moreover, the addition of RPs reduced the compressive strength, and this effect was more evident for RRAC-B. For RA replacement ratios of 50 and 100%, the compression strength of RRAC with 5, 10, and 15% rubber content was 7.26, 8.53, 11.07, and 4.86, 11.38, and 19.47% lower than that of recycled concrete without rubber, respectively.

Considering the elastic properties, the content of rubber and replacement ratio of RA have little effect on Poisson's ratio, which is stable at approximately 0.2. As shown in **Figure 4B**, the experimental results showed that for a RA replacement ratio of 50%, the elastic modulus of RRAC-A-5 was 2.95% lower than that of the natural aggregate concrete (RNAC-5), whereas the elastic modulus of recycled aggregate was 8.82% lower than that of RNAC-5 for RA replacement ratio of 100%. Moreover, the elastic modulus of RRAC with various rubber contents (5, 10, and 15%) decreased by 1.91, 5.69, and 9.32% for the same RA replacement ratio (50%), respectively. A similar trend was observed for 100% replacement rate of recycled aggregate. Therefore, the elastic modulus of RRAC decreased with an increase in the RA replacement ratio and rubber content.

### Failure Modes

Typical failure modes of specimens after the uniaxial compression test are shown in **Figure 5**. The crack width was found to increase with the RA replacement rate, because, in contrast to NAC, RAC is comprised of five-phase media—NA, old mortar of RA, new mortar, old interfacial transition zone (ITZ) between old mortar and NA, and new ITZ between the new and old mortar (Lee and Choi, 2013). In addition, a large number of microcracks and pores were produced in the production process of RA owing to transport impacts (Nagataki et al., 2004; Tam et al., 2005). The strength of the new ITZ between the new and old mortar was reduced owing to the formation of a water film covering the surface of RA resulting from the high water absorption of RA. Furthermore, the crack growth developed along the weak zones of the RAC more easily. Therefore, an increase in the RA replacement ratio slightly reduced the compression strength of RRAC.

On the contrary, the number and width of the cracks decreased with the increase in the rubber content for the same RA replacement ratio, as shown in **Figure 5**. As concrete is a type of brittle material, cracks are usually generated through tensile strain when compression loads are applied. The RPs were used as soft materials to fill the microcracks and pores in the RAC; thus, the addition of rubber inhibited the expansion of a number of cracks and enhanced the deformation capacity of specimens.



### Stress–Strain Relationship

The stress–strain curves of the RRAC are depicted in **Figure 6**, where **Figure 6A** illustrates that the stress–strain curves of RRAC

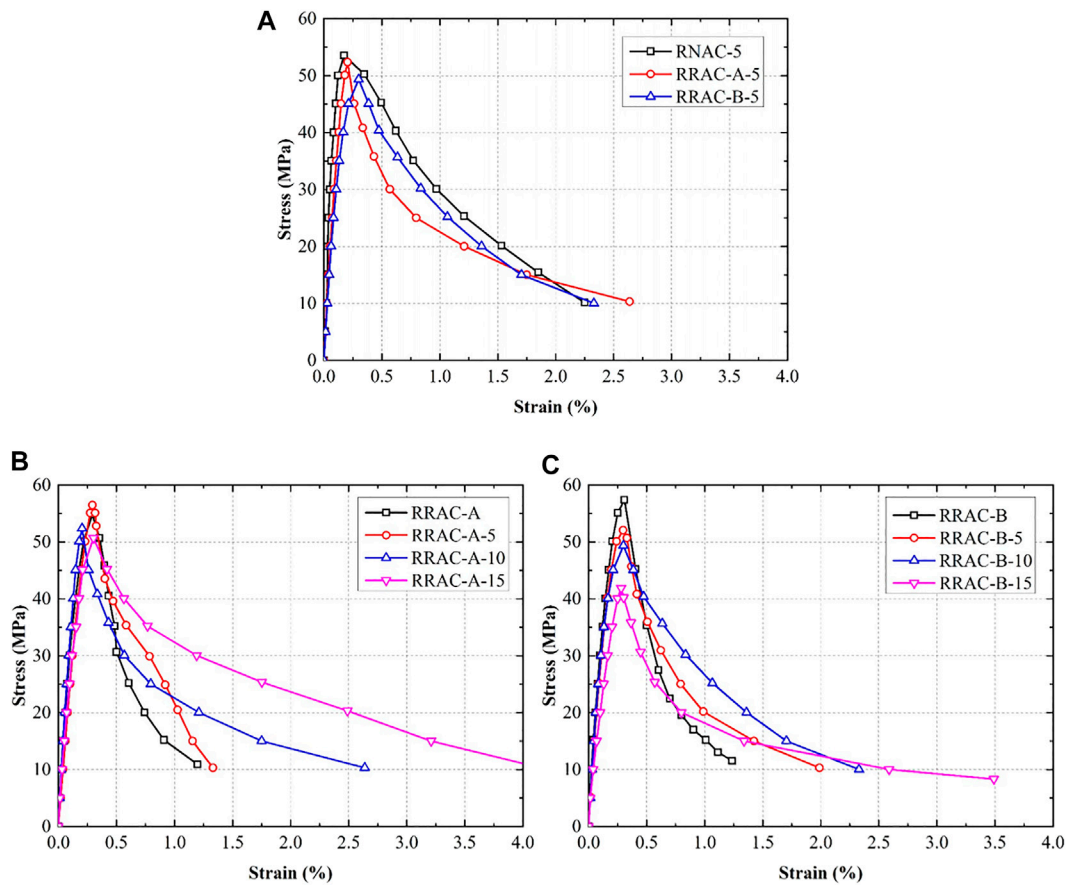


**FIGURE 6** | Stress–strain curves of RRAC: **(A)** 5% rubber content; **(B)** RRAC-A; **(C)** RRAC-B.

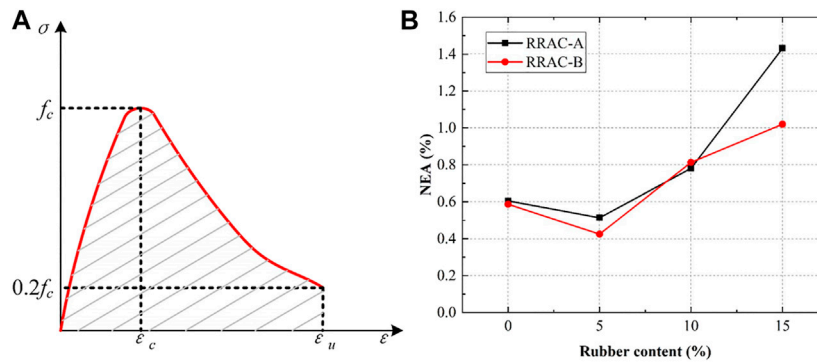


**FIGURE 7** | Calculation method and NEA of RRAC: **(A)** Calculation method of energy absorption; **(B)** NEA of RRAC under different rubber content.

**TABLE 5** | Energy absorption (EA) and normalized energy absorption (NEA).

	RRAC-5	RRAC-A	RRAC-A-5	RRAC-A-10	RRAC-A-15	RRAC-B	RRAC-B-5	RRAC-B-10	RRAC-B-15
EA (MPa)	0.66	0.35	0.27	0.42	0.72	0.32	0.22	0.44	0.45
NEA (%)	1.81	0.61	0.51	0.78	1.43	0.59	0.43	0.89	1.02

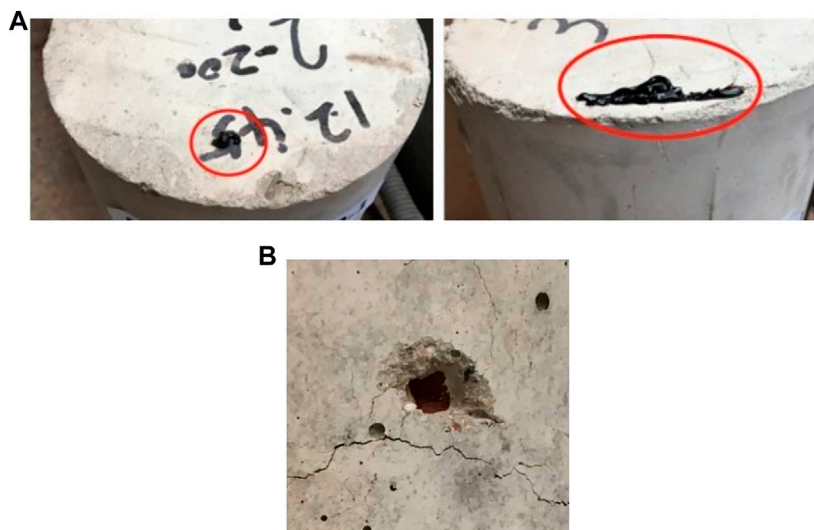


**FIGURE 8 | (A)** Melting rubber escaping through pores and cracks; **(B)** Spalling on the surface of RAC after high-temperature treatment (600°C).

are slightly different from those of RNAC. The falling section in the stress–strain curve of RRAC could be prolonged by mixing RPs, and a higher rubber content corresponded to a larger ultimate strain; therefore, the RPs could improve the deformation ability of RAC, as depicted in **Figures 6B,C**.

### Energy Absorption Capacity

The area surrounded by the stress–strain curve represents the energy absorption of the specimens in the compression test. Several scholars have employed this method to evaluate the energy absorbing ability of concrete during the process of compression deformation. The specimen was close to failure in the later stage of stress unloading owing to the brittleness of the concrete material; thus, the strain corresponding to 20% peak stress ( $0.2f_c$ ) was defined as the ultimate strain  $\epsilon_u$ , as shown in **Figure 7A**. However, both RPs and RAs combinedly influenced the uniaxial compressive strength. Therefore, the energy absorption (EA) capacity of all specimens was normalized (NEA) with their compression strengths and are summarized in **Table 5**. In comparison to RNAC, the incorporation of RA reduced the energy absorption capacity of concrete. In addition, the energy absorption capacity of RRAC increased gradually with the rubber content, and it was unchanged for a rubber content less than 5%, as shown in **Figure 7B**. This phenomenon is consistent with existing results (Ganjian et al., 2009), which indicates that the performance of concrete cannot be evidently improved with small rubber content. In other words, more than 5% rubber content could enhance the toughness of RAC.

### RRAC After Heated at High Temperature Surface Observation

The door of the box resistance furnace manual opens when the internal temperature reaches a certain temperature to facilitate the observation of the phenomena occurring during the process at

elevated temperatures. During the heating treatment, a small amount of water vapor began to escape beyond 100°C, and the steam escape was more evident when the temperature gradually increased to 160°C. In addition, the RPs started to melt and escape through the pores and cracks in the concrete, as shown in **Figure 8A**. The release of water vapor gradually decreased at elevated temperatures of 300°C, but a strong irritant smell still

**TABLE 6 |** Mass loss for RRAC.

Target temperature (°C)	Specimen No	Mass loss (%)
200	RNAC-5-200	3.42
	RRAC-A-200	3.58
	RRAC-A-5-200	4.14
	RRAC-A-10-200	3.52
	RRAC-A-15-200	3.91
	RRAC-B-200	3.65
	RRAC-B-5-200	3.29
	RRAC-B-10-200	3.53
	RRAC-B-15-200	3.51
	400	RNAC-5-400
RRAC-A-400		6.19
RRAC-A-5-400		6.14
RRAC-A-10-400		6.76
RRAC-A-15-400		6.40
RRAC-B-400		6.23
RRAC-B-5-400		6.90
RRAC-B-10-400		7.44
RRAC-B-15-400		7.28
600		RNAC-5-600
	RRAC-A-600	7.63
	RRAC-A-5-600	7.32
	RRAC-A-10-600	7.94
	RRAC-A-15-600	8.10
	RRAC-B-600	7.73
	RRAC-B-5-600	8.66
	RRAC-B-10-600	9.32
	RRAC-B-15-600	8.78

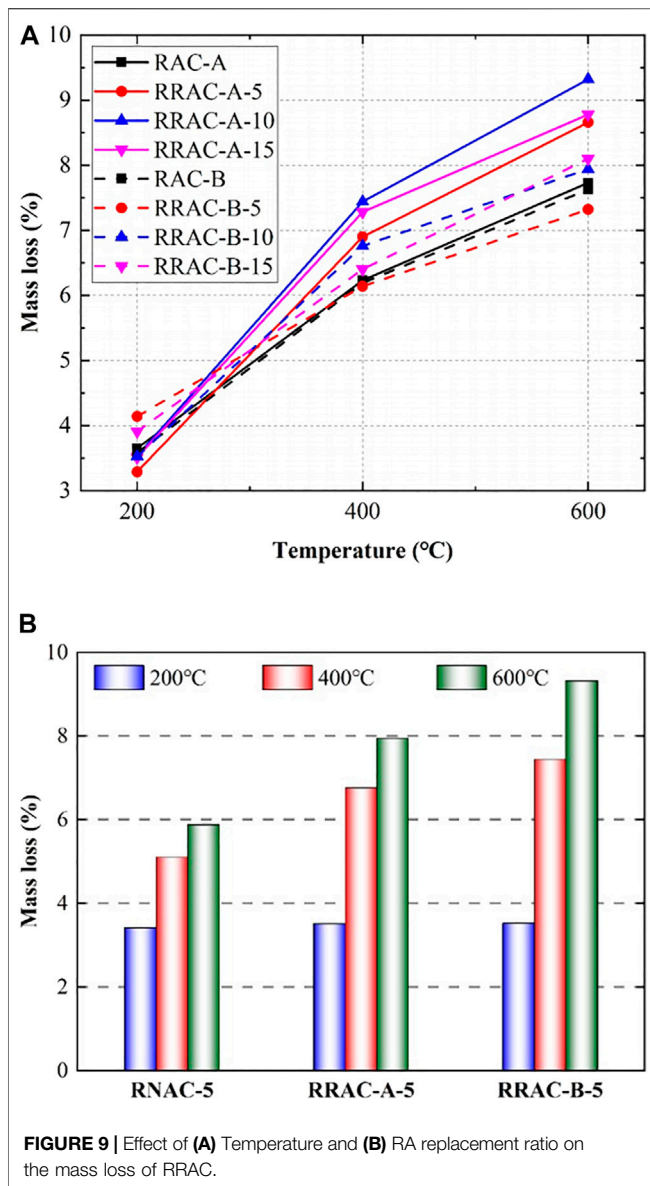


**FIGURE 9 |** Effect of (A) Temperature and (B) RA replacement ratio on the mass loss of RRAC.

persisted because most of the RPs had melted. However, a small amount of steam still escaped from the edges of the furnace door upon attainment of the target temperature. The specimen was removed for practical observation after completion of the heating treatment.

The aggregate, mortar, and rubber in the concrete underwent a series of changes under high temperatures. From a macro level, these changes mainly depict the development of cracks and change in color of the cylindrical surface. At a high temperature of 600 C, numerous microcracks interlaced with each other and the lightest color of the specimens were observed; certain specimens without rubber modification (RAC-A and RAC-B) exhibited small areas of spalling on the surface, as illustrated in **Figure 8B**. Therefore, the experimental phenomena demonstrated that RPs could reduce the spalling of RAC.

## Mass Loss

As explained earlier, the specimens were weighed before and after the heating treatment,  $m_0$  and  $m_1$ , respectively. Moreover, the surfaces of the specimens were cleaned after the heat treatment. Thus, the mass loss,  $\beta$ , can be calculated as shown in **Eq. 2**. The results are summarized in **Table 6**. As shown in **Figure 9A**, the melting rubber broadened the escaping channel for internal water vapor. Therefore, the mass loss of RRAC increased with an increase in the rubber content. On the contrary, the mass loss of RNAC and RRAC was similar after heating treatment at 200 C under the same rubber content, as shown in **Figure 9B**. In comparison to RNAC after the heating treatment at 400°C, the mass loss for RRAC with 50% RA and 100% RA replacement ratio increased by 32.29 and 45.60%, respectively. The difference in mass loss between RRAC and RNAC was greater (35.03 and 58.50%, respectively) after heating treatment at 600°C. According to *Failure Modes*, there were more pores and microcracks in the RAC (Nagataki et al., 2004; Tam et al., 2005) to let water vapor escape.

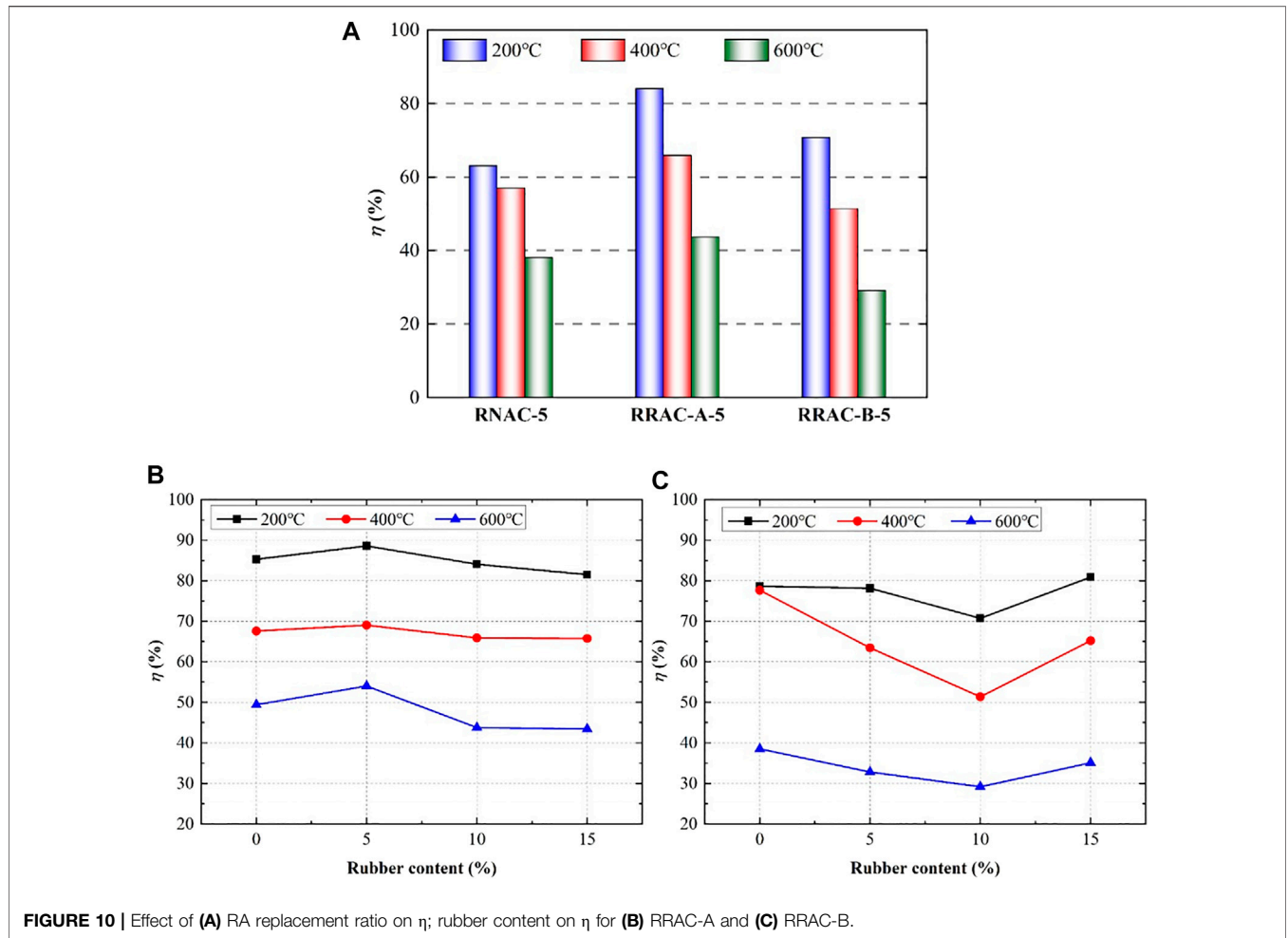
$$\beta = \frac{m_1 - m_2}{m_0} \times 100 \% \quad (2)$$

## Residual Uniaxial Compression Strength

After the observation of the specimen surface and the measurement of mass loss, compression tests of all heated specimens were carried out using the universal testing machine. The uniaxial residual compression strength  $f_{cr}$  is listed in **Table 7**, where  $\eta$  represents the ratio of compression strength post heat treatment to that at ambient temperature (25°C). As shown in **Figure 10A**, after heating at 200, 400, and 600°C for a duration, the residual uniaxial compression strength of RRAC-A-5 was 33.28, 15.67, and 14.92% higher than that of RNAC-5. The pores in the RAs could provide the vapor escape channels at high temperatures to reduce the damage caused by internal vapor pressure, unlike that in RNAC. However, the defects of the aggregate itself adversely affect the

**TABLE 7 |** Residual compression strength after heating.

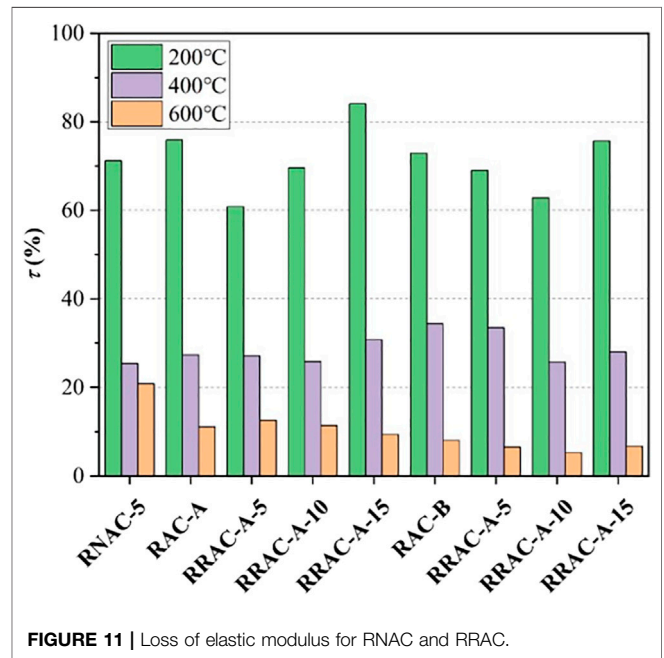
	25°C		200°C		400°C		600°C	
	$f_c$ (MPa)	$\eta$ (%)	$f_{cr}$ (MPa)	$\eta$ (%)	$f_{cr}$ (MPa)	$\eta$ (%)	$f_{cr}$ (MPa)	$\eta$ (%)
RNAC-5	54.38	63.08	34.30	30.99	56.98	20.71	38.08	
RAC-A	57.18	85.27	48.76	38.65	67.59	28.26	49.42	
RRAC-A-5	53.03	88.57	46.97	36.61	69.04	28.65	54.03	
RRAC-A-10	52.30	84.07	43.97	34.47	65.91	22.89	43.76	
RRAC-A-15	50.85	81.49	41.44	33.43	65.74	22.09	43.43	
RAC-B	55.61	78.62	43.72	43.18	77.65	21.42	38.52	
RRAC-B-5	52.91	78.13	41.34	33.58	63.46	17.36	32.82	
RRAC-A-5	49.28	70.75	34.86	25.32	51.38	14.38	29.17	
RRAC-A-10	44.78	80.91	36.23	29.20	65.21	15.72	35.11	
RRAC-A-15								



**TABLE 8 | Elastic modulus after heating treatment.**

	25 °C		200 °C		400 °C		600 °C	
	<i>E</i> (MPa)	<i>E<sub>r</sub></i> (MPa)	$\tau$ (%)	<i>E<sub>r</sub></i> (MPa)	$\tau$ (%)	<i>E<sub>r</sub></i> (MPa)	$\tau$ (%)	
RNAC-5	30.50	21.70	71.15	7.74	25.39	6.35	20.82	
RAC-A	31.87	24.17	75.85	8.72	27.36	3.54	11.12	
RRAC-A-5	31.26	19.01	60.80	8.47	27.08	3.94	12.59	
RRAC-A-10	29.60	20.59	69.55	7.64	25.80	3.37	11.39	
RRAC-A-15	28.90	24.31	84.12	8.88	30.74	2.71	9.38	
RAC-B	28.87	21.04	72.89	9.91	34.33	2.33	8.05	
RRAC-A-5	27.91	19.27	69.04	9.34	33.48	1.83	6.54	
RRAC-A-10	27.81	17.46	62.80	7.15	25.70	1.47	5.27	
RRAC-A-15	26.38	19.96	75.66	7.39	28.00	1.78	6.73	

ITZ of the concrete in case of high RA replacement ratios (100%). Therefore, the trend of  $\eta$  for RA replacement initially increased first but later declined.



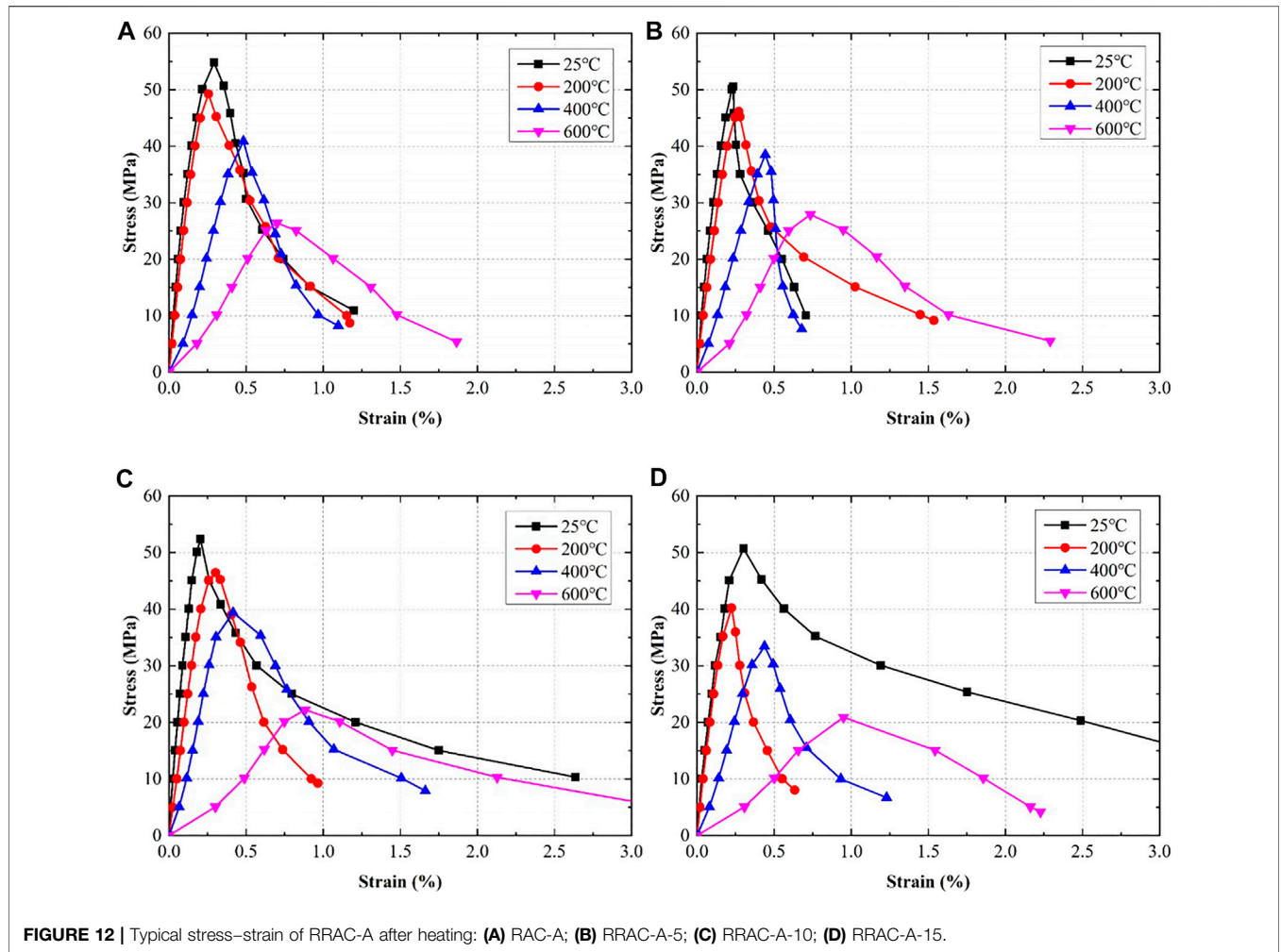


FIGURE 12 | Typical stress–strain of RRAC-A after heating: (A) RAC-A; (B) RRAC-A-5; (C) RRAC-A-10; (D) RRAC-A-15.

On the contrary, the residual compression strength of concrete initially increased with the rubber content for 50% RA replacement rate (RRAC-A) but declined afterward, as shown in Figures 10B,C. The reason is that the RPs melted at high temperatures, which provided more channels to release the water vapor, thus reducing the internal damage and burst caused by the vapor pressure. Similar to RA, the porosity of a specimen with significant rubber content increased after the heat treatment owing to the melting of the rubber making the internal structure of concrete loose. The specimen with 100% RA replacement rate (RRAC-B) exhibited the highest porosity, and these small pores could easily connect to form larger pores after the rubber melted. Therefore, the porosity of concrete did not vary linearly with the heat resistance.

By conducting the multiple nonlinear regression (MNR) analysis, the value of  $\eta$ , as a function of target temperature  $T$  (°C) and rubber content  $\omega$  (%) can be calculated by Eq. 3 proposed by Akbarzadeh Bengar et al. (Akbarzadeh Bengar et al., 2020):

$$\eta = \frac{a - (bT + c\omega)}{1 + dT - e\omega} \quad (25 \leq T \leq 600^\circ\text{C}; 0 \leq \omega \leq 15\%) \quad (3)$$

where  $a$ ,  $b$ ,  $c$ ,  $d$ , and  $e$  are the undetermined coefficients, which are found as 1.022,  $9.153 \times 10^{-4}$ , 0.008,  $-1.391 \times 10^{-4}$ , 0.008 for

RRAC-A, 1.013,  $1.190 \times 10^{-3}$ , 0.005,  $-3.675 \times 10^{-4}$ , 0.003 for RRAC-B, respectively. In addition, the fits of goodness ( $R^2$ ) for RRAC-A and RRAC-B are 0.991 and 0.941, respectively. In other words, this equation agrees well with the experimental data.

TABLE 9 | Energy absorption (EA) and normalized energy absorption (NEA) after heating.

	200°C		400°C		600°C	
	EA (MPa)	NEA (%)	EA (MPa)	NEA (%)	EA (MPa)	NEA (%)
RRAC-5	0.29	0.85	0.25	0.81	0.31	1.50
RAC-A	0.30	0.62	0.28	0.72	0.24	0.85
RRAC-A-5	0.25	0.53	0.24	0.66	0.23	0.80
RRAC-A-10	0.21	0.48	0.30	0.87	0.14	0.61
RRAC-A-15	0.26	0.63	0.25	0.75	0.21	0.95
RRAC-B	0.25	0.57	0.23	0.53	0.17	0.79
RRAC-A-5	0.19	0.46	0.19	0.57	0.16	0.92
RRAC-A-10	0.17	0.49	0.15	0.59	0.13	0.90
RRAC-A-15	0.26	0.72	0.21	0.72	0.15	0.95

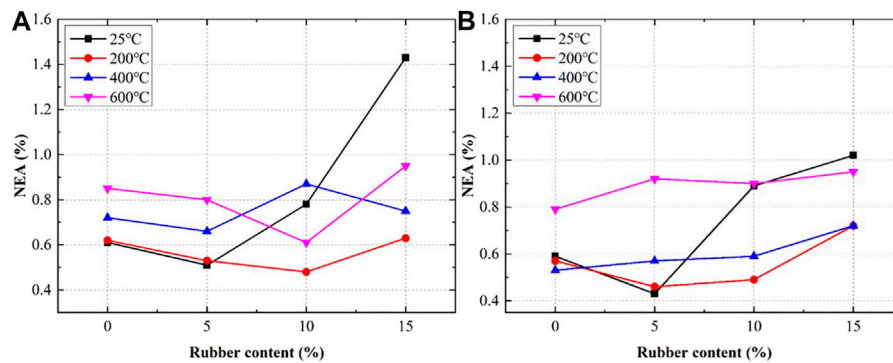


**FIGURE 13** | Effect of rubber content on the NEA of (A) RRAC-A and (B) RRAC-B.

### Residual Elastic Modulus

The residual elastic modulus is summarized in **Table 8**, where  $\tau$  represents the ratio of the residual elastic modulus  $E_r$  at high temperatures to the elastic modulus at room temperature. As shown in **Figure 11**, the effect of rubber content on the elastic modulus of RRAC after heating beyond 400°C was smaller than that at room temperature, and the degradation of elastic modulus at a high temperature cannot be significantly reduced with addition of rubber.

By conducting the MNR analysis, the value of  $\tau$ , as a function of target temperature  $T$  (°C) and rubber content  $\omega$  (%) can be calculated by:

$$\tau = \frac{a - (bT + c\omega)}{1 + dT - e\omega} \quad (25 \leq T \leq 600^\circ\text{C}; 0 \leq \omega \leq 15\%) \quad (4)$$

where  $a$ ,  $b$ ,  $c$ ,  $d$ , and  $e$  are found as  $1.051$ ,  $1.580 \times 10^{-3}$ ,  $-1.230 \times 10^{-3}$ ,  $6.446 \times 10^{-4}$ ,  $1.620 \times 10^{-3}$  for RRAC-A, and  $1.061$ ,  $1.610 \times 10^{-3}$ ,  $3.610 \times 10^{-3}$ ,  $4.481 \times 10^{-4}$ ,  $3.650 \times 10^{-3}$  for RRAC-B, respectively. In addition, the fits of goodness ( $R^2$ ) for RRAC-A and RRAC-B are 0.968 and 0.989, respectively. In other words, this equation agrees well with the experimental data.

### Failure Modes

The failure modes of RRAC with different rubber contents and RA replacement ratios were observed to be similar; therefore, only the compressive failure modes beyond the 600°C heating treatment are shown in **Figure 5B**. The specimens experiencing a high temperature of 600°C exhibited cracks earliest in the loading process and suffered the most severe damage among others. The cracks were mainly developed along the interface between the aggregate and mortar. Thus, the cohesive force of the aggregate was significantly reduced leading to the collapse of the specimen in a large area.

### Stress–Strain Curves

The compressive behaviors of all the specimens after the heat treatment were determined using the compression testing machine. Considering RRAC-A as an example, the stress–strain curves are plotted in **Figure 12**. The stiffness (slope of the rising phase of the curve) of all specimens treated at 200°C almost coincided with that of specimens treated at room temperature.

The stiffness decreased as the heating temperature increased beyond 200°C, i.e., at 400 and 600°C, because of the melting temperatures are starting at around 160°C of the rubber as mentioned in **Section 3.2.1**. After heating at high temperatures, more microcracks and pores were produced in the concrete. Consequently, calcium hydroxide—the main part of the hydration products of concrete (Li et al., 2004)—started to decompose beyond temperatures of 400°C. These pores enhanced the deformation ability of the concrete resulting in extension of the ultimate strain limits of the stress–strain curves.

### Residual Energy Absorption Capacity

The values of EA and NEA can be calculated based on the stress–strain curves, as shown in **Table 9**. As shown in **Figure 13**, in contrast to the EA at room temperature, a higher temperature corresponded to a less concrete-toughening effect of the rubber owing to decomposition of rubber at high temperature; moreover, the NEA of RRAC remained stable for different rubber contents. Additionally, from the perspective of the RA replacement ratio, the effect of RPs on RRAC-B was more remarkable than that of RRAC-A. In other words, the rubber content should be increased with respect to the RA replacement ratio.

### Constitutive Model for RRAC With Temperature and Rubber Content

#### Review of the Constitutive Model for RAC

As analyzed in *Stress–Strain Relationship* and *Stress–Strain Curves*, the constitutive curve of RAC was similar to that of ordinary concrete in terms of its geometric characters. One of the common constitutive models is illustrated in the Chinese standard GB50010 (GB/T 50010-2010, 2015), as shown in **Eq. 5**.

$$\begin{cases} y = a_0 + a_1x + a_2x^2 + a_3x^3 & x \leq 1 \\ y = \frac{x}{b_0 + b_1x + b_2x^2} & x > 1 \end{cases} \quad (5)$$

where  $y = \sigma/f_c$ ;  $\sigma$  is the uniaxial compression stress;  $f_c$  is the peak stress under uniaxial compression;  $x = \varepsilon/\varepsilon_c$ ;  $\varepsilon$  is the strain under uniaxial compression;  $\varepsilon_c$  is the strain corresponding to the peak stress under uniaxial compression;  $a_i$  ( $i = 0, 1, 2, 3$ ) and  $b_j$  ( $j = 0, 1, 2$ )

are the undetermined coefficients. The constitutive curve of concrete has some common features, as follows:

- 1) The curve starts at (0,0) when  $x = 0, y = 0$ .
- 2) The slope of the ascending segment of the curve decreases gradually without any inflection point for  $0 \leq x < 1, d^2y/dx^2 < 0$ .
- 3) For  $x = 1, y = 1$ , and  $dy/dx = 0$ , the curve has only one peak point.
- 4) When  $x > 1$ , there is an inflection point  $(x_1, y_1)$  in the descending segment and  $d^2y/dx^2 = 0$ .
- 5) When  $x > x_1$ , there is a maximum curvature point  $(x_2, y_2)$ ,  $d^3y/dx^3 = 0$ .
- 6) When  $x \rightarrow \infty, y \rightarrow 0, dy/dx \rightarrow 0$ , which means that the descending curve is infinitely close to the X-axis but does not intersect.
- 7) For the entire curve,  $x$  is always greater than 0 and  $y$  is always between 0 and 1.

Therefore, the ascending and descending segments of the curve can be simplified based on these features and expressed as (Li et al., 2014):

$$\begin{cases} y = ax + (3 - 2a)x^2 + (a - 2)x^3 & x \leq 1 \\ y = \frac{x}{b(x - 1)^2 + x} & x > 1 \end{cases} \quad (6)$$

where  $a$  and  $b$  are the undetermined coefficients. Currently, there are relatively few studies on the stress-strain curves of RAC. Most of the fitting analysis of the curve focuses on concrete with different RA replacement rates at room temperature. Therefore, the constitutive models of RRAC-A and RRAC-B should be studied in variance of temperature and rubber content.

### Constitutive Model for RRAC With Temperature and Rubber Content

Equation 6 was used for nonlinear fitting of the stress-strain curve of RRAC, and the undetermined coefficients were determined and summarized in Table 10. The goodness of fit ( $R^2$ ) was determined at above 0.9, thus verifying the suitability of this model for RRAC.

Furthermore, the constitutive model of RRAC-A and RRAC-B can be integrated with different target temperatures and rubber contents using the parameters  $a$  and  $b$ , as expressed in Eqs. 7,8, where  $T$  (°C) and  $w$  (%) represent the target temperature and the rubber content, respectively. The fitting results are shown in Figure 14. Therefore, all the undetermined coefficients for RRAC-A and RRAC-B were evaluated in Eqs. 9, 11, 12, respectively. As there were only two RA replacement rates in this investigation and there was a certain dispersion of the stress-strain curve after the high-temperature damage, the unification of RRAC-A and RRAC-B was difficult. Thus, a larger size of additional test data including more number of RA replacement ratios are needed for further study.

$$a = a_0 + a_1T + a_2w + a_3T^2 + a_4w^2 + a_5wT \quad (7)$$

TABLE 10 | Parameters fitting of the constitutive model for RRAC.

RAC-A	Temperature (°C)			
	25	200	400	600
$a$	1.9312	1.3013	0.2915	-0.1560
$R^2$	0.9990	0.9990	0.9996	0.9928
$b$	2.1061	1.2063	5.6603	6.3729
$R^2$	0.9886	0.9869	0.9909	0.9962
RRAC-A-5	Temperature (°C)			
	25	200	400	600
$a$	1.1224	1.2722	0.0730	-0.2712
$R^2$	0.9969	0.9980	0.9836	0.9988
$b$	1.1529	1.7726	4.6394	2.2241
$R^2$	0.9350	0.8900	0.9974	0.9769
RRAC-A-10	Temperature (°C)			
	25	200	400	600
$a$	1.3280	0.9052	0.1455	-0.3776
$R^2$	0.9956	0.9998	0.9942	0.9924
$b$	0.5406	0.7177	1.4424	1.6870
$R^2$	0.8910	0.9834	0.9885	0.9944
RRAC-A-15	Temperature (°C)			
	25	200	400	600
$a$	1.7635	1.2841	0.3343	-0.2680
$R^2$	0.9967	0.9978	0.9982	0.9951
$b$	0.3059	0.5942	2.5183	2.8356
$R^2$	0.9271	0.9908	0.9926	0.9121
RRAC-B	Temperature (°C)			
	25	200	400	600
$a$	1.9762	0.9889	0.4839	-1.0052
$R^2$	0.9977	0.9972	0.9992	0.9792
$b$	2.1374	11.8842	2.4468	5.2808
$R^2$	0.9618	0.9331	0.9451	0.9580
RRAC-B-5	Temperature (°C)			
	25	200	400	600
$a$	1.8258	1.2670	0.6951	0.0500
$R^2$	0.9999	0.9995	0.9972	0.9994
$b$	1.1220	3.1048	19.6305	3.6717
$R^2$	0.9523	0.9944	0.9367	0.9722
RRAC-B-10	Temperature (°C)			
	25	200	400	600
$a$	2.1821	0.9115	0.6813	0.3862
$R^2$	0.9997	0.9985	0.9994	0.9991
$b$	0.5866	3.8111	3.9843	0.6735
$R^2$	0.9775	0.9593	0.9863	0.9364
RRAC-B-15	Temperature (°C)			
	25	200	400	600
$a$	1.3001	1.9879	1.4802	-0.0431
$R^2$	0.9900	0.9998	0.9934	0.9940
$b$	0.8778	1.0172	1.3355	2.6404
$R^2$	0.9033	0.9889	0.9045	0.9645

$$b = b_0 + b_1T + b_2w + b_3T^2 + b_4w^2 + b_5wT \quad (8)$$

$$a = 1.860 - 0.003T - 0.091w - 1.983 \times 10^{-7}T^2 + 0.006w^2 + 1.836 \times 10^{-6}wT \quad (9)$$

$$b = 1.700 + 0.009T - 0.379w - 2.889 \times 10^{-6}T^2 + 0.198w^2 - 2.601 \times 10^{-4}wT \quad (10)$$

$$a = 1.856 - 0.003T + 0.020w - 2.667 \times 10^{-6}T^2 - 0.002w^2 + 1.526 \times 10^{-4}wT \quad (11)$$

$$b = 1.219 + 0.008T + 0.194w - 9.747 \times 10^{-6}T^2 - 0.019w^2 + 1.177 \times 10^{-4}wT \quad (12)$$

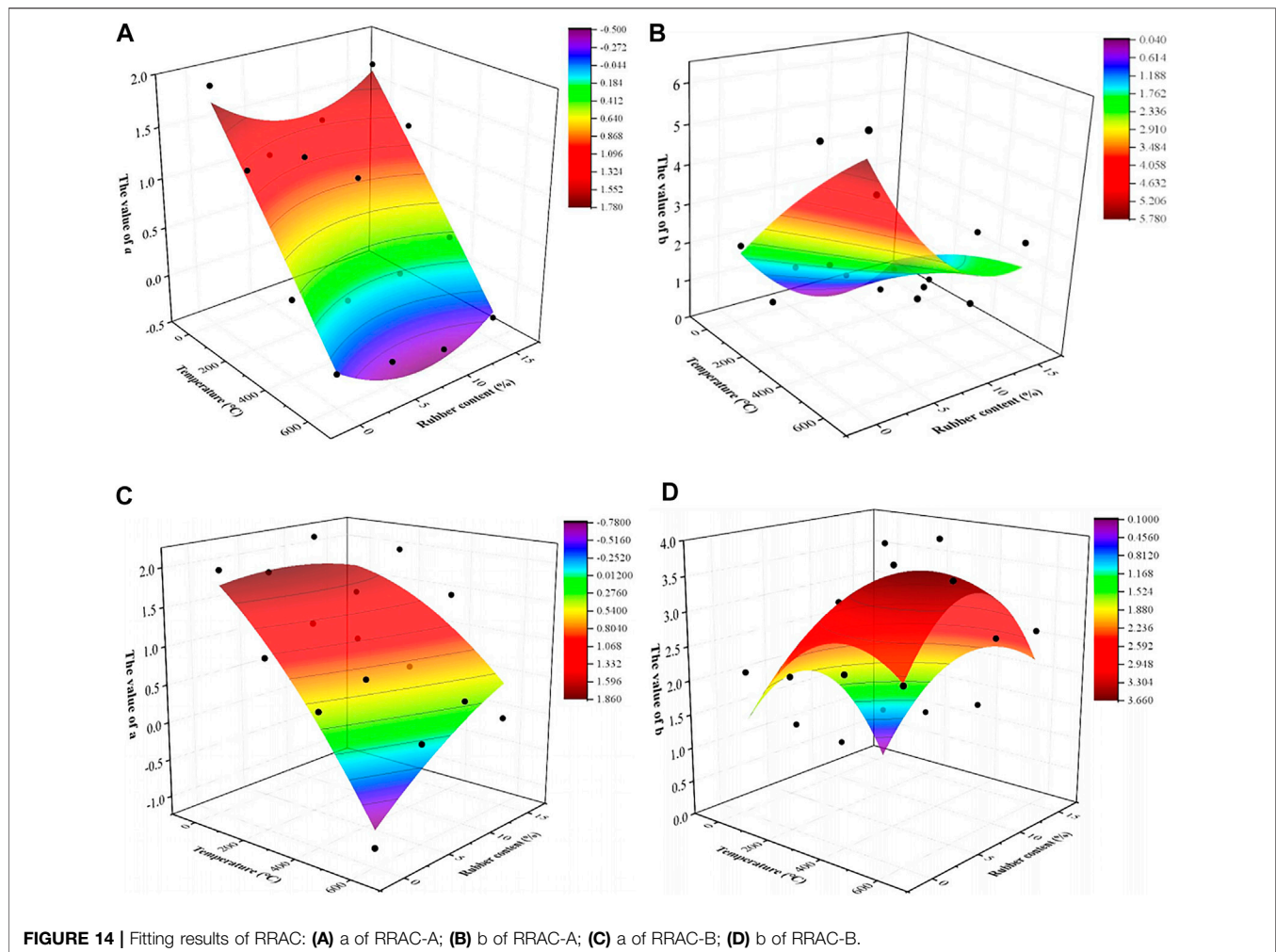


FIGURE 14 | Fitting results of RRAC: (A) a of RRAC-A; (B) b of RRAC-A; (C) a of RRAC-B; (D) b of RRAC-B.

## MICROSTRUCTURE AND SPALLING MECHANISM ANALYSIS

### RRAC Specimens at Ambient Temperature (25°C)

There were multiple microcracks between the rubber particle and mortar, as depicted in **Figure 15A**, indicating that the transition interface was relatively weak. Therefore, the compressive strength of the concrete weakened with the increase in rubber content. In addition, as shown in **Figures 15A,B** variety of cement hydration products was observed in the cementing materials, among which there were numerous ettringite formation (AFt), and a compact structure was formed to connect the surrounding products. Moreover, a small amount of calcium hydroxide (CH) was observed, and microcracks developed along the weak interface between the mortar and aggregate.

### RRAC Specimens After Heated at 200°C for 60 min

As shown in **Figure 15C**, RPs only softened and did not decompose after heating at 200°C; therefore, there was no

noticeable change in morphology. In addition, cracks had developed along the weak interface. Compared with the samples at ambient temperature, the cracks were longer and wider at higher temperatures, indicating that the damage inside the concrete was more extensive owing to heating. Further, **Figure 15D** confirms the absence of AFt in RRAC at high temperatures because AFt had completely decomposed at 200°C. However, calcium silicate hydrate (C-S-H) and CH were not decomposed at this temperature. Therefore, the positive influence of the RRAC was relatively small after heating at 200°C.

### RRAC Specimens After Heated at 400°C for 60 min

As depicted in **Figure 15E**, since almost all RPs have been decomposed, no RPs can be found at 400°C. Several holes are formed in the place initially occupied by the cracking and escaping rubber in the cementitious paste. As depicted in **Figure 15F**, there was an adverse change in the microstructure of the specimen, and the amount of cement hydration products (such as AFt and CH) had dramatically

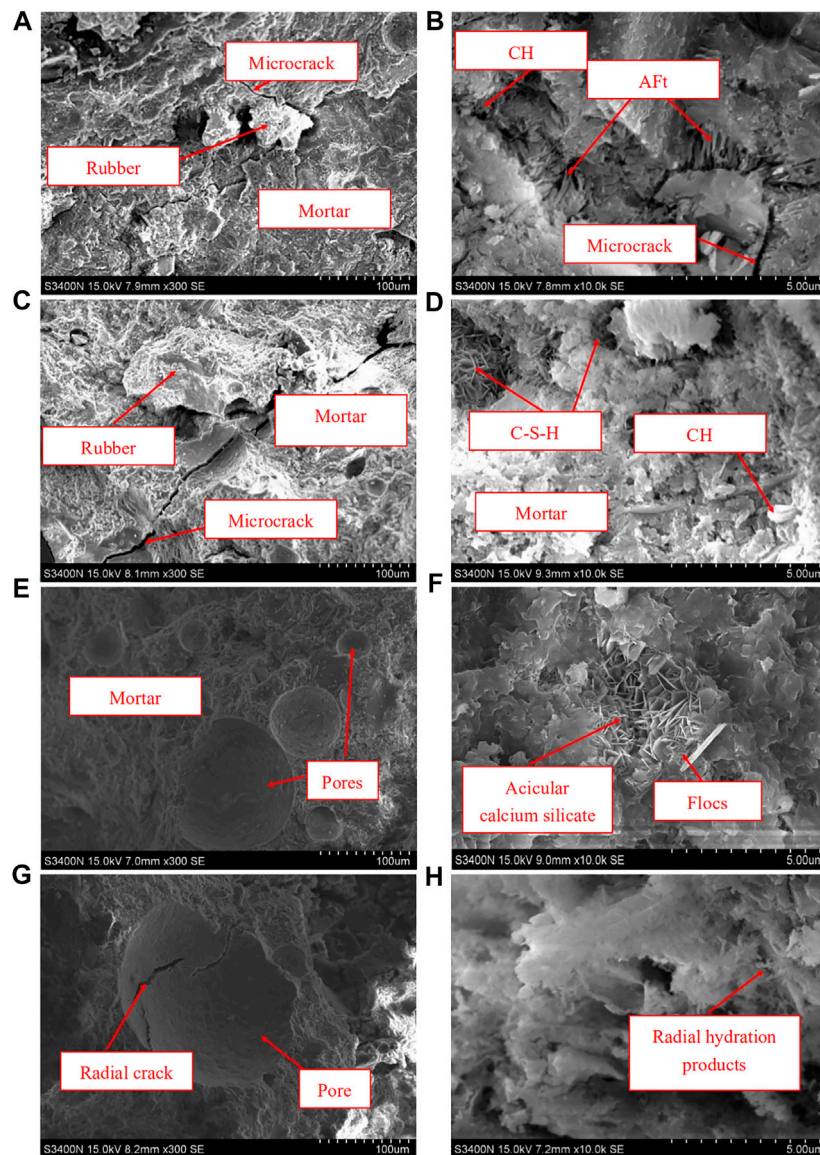


**FIGURE 15 |** Microstructure of RRAC: (A) and (B) 25°C; (C) and (D) 200°C; (E) and (F) 400°C; (G) and (H) 600°C.

reduced. The cement hydration products decomposed into acicular calcium silicate and flocs.

### RRAC Specimens After Heated at 600°C for 60 min

As shown in **Figure 15G**, few holes were still present in the microstructure by the RPs after heating at 600°C, but the damage of concrete caused by this high temperature was the most severe among all the cases. In addition, these holes provided space for the development of cracks that penetrated each other to form even larger cracks. As shown in **Figure 15H**, only few radial hydration products were present, which were the residual hydration products of mortar after decomposition at high temperatures. In addition, these radial hydration products led to radial cracks in the ITZ.

### Spalling Mechanism Under Elevated Temperatures for RRAC

A large amount of water evaporated from the cement paste at temperatures below 400°C, and all kinds of hydration products decomposed successively. Although the pressure inside the structure increased according to the vapor pressure theory, the internal pores and the escaping of RPs released the space within the structure. In other words, the internal vapor pressure was effectively released from the dense concrete structure under the influence of the increased rubber content that created more space. On the contrary, almost all the hydration products of the cement decomposed and the crystal water escaped from the aggregate upon reaching 600°C. Simultaneously, the mismatch responses between aggregates

and mortar led to thermal stresses in the ITZ owing to the thermal expansion of materials. Although a high rubber content released a large amount of space under elevated temperatures and provided a buffer to the steam pressure, the load capacity was decreased owing to the relatively loose internal structure of RRAC compared to that of ordinary concrete. Therefore, the rubber content should not be too high considering the strength and spalling resistance of RRAC.

## CONCLUSION

Uniaxial compressive tests on RRAC specimens with two RA replacement rates (50 and 100%), three rubber contents (0, 5, 10, and 15%), and four temperatures (25, 200, 400, and 600°C) were conducted to explore the properties of the concrete media. The RRAC was found as a suitable alternative to the RAC for use in structures requiring fire resistance. The following conclusions can be drawn from the investigation:

RRAC is a type of low-carbon building material compared to ordinary concrete, where the CO<sub>2</sub> emissions slightly decrease because the amount of sand is reduced with a higher rubber content in the mix. Approximately 1 kg of carbon dioxide can be reduced in the process of producing one cubic concrete upon complete replacement of NAs with RAs.

Between the completion of heat treatment and performing the compression test, a small area of spalling was observed on the surface of certain specimens, except for the rubberized specimens. In addition, the melting rubber broadened the escaping channel for releasing the internal water vapor. Therefore, the mass loss of RRAC increased with an increase in rubber content.

With an increase in temperature, the effect of rubber content on the elastic modulus of RRAC was smaller than that at room temperature. Consequently, more number of microcracks and pores were produced in the concrete after heating at high temperatures beyond 400°C. These pores enhanced the deformation ability of concrete and extended the ultimate strain limit of the stress–strain curves.

Unlike the energy absorption capacity at room temperature, the toughening effect of rubber on concrete was lessened at higher temperatures owing to the decomposition of rubber at such temperatures.

## REFERENCES

- Ahmed, W., and Lim, C. W. (2021). Production of sustainable and structural fiber reinforced recycled aggregate concrete with improved fracture properties: a review. *J. Clean. Prod.* 279, 123832. doi:10.1016/j.jclepro.2020.123832
- Akbarzadeh Bengar, H., Shahmansouri, A. A., Akkas Zangebari Sabet, N., Kabirifar, K., and W.Y. Tam, V. V. (2020). Impact of elevated temperatures on the structural performance of recycled rubber concrete: experimental and mathematical modeling. *Construction Building Mater.* 255, 119374. doi:10.1016/j.conbuildmat.2020.119374
- Albano, C., Camacho, N., Reyes, J., Feliu, J. L., and Hernández, M. (2005). Influence of scrap rubber addition to Portland I concrete composites: destructive and non-destructive testing. *Compos. Structures* 71, 439–446. doi:10.1016/j.compstruct.2005.09.037

Empirical models were proposed to reflect the effects of high temperature and rubber contents on the stress–strain relationship of RRAC.

Based on the microstructure analysis using SEM, numerous pores were observed that facilitated the release of internal vapor through the cracking and escaping rubber. Moreover, the RPs could reduce the spalling of specimens based on the vapor pressure theory. Thus, RRAC with 10% rubber was recommended on considering the factors of uniaxial compressive strength, energy absorption capacity, and spalling resistance.

## Scope for Future Research

- 1) There are limit data about the stress-strain relations of RRAC under the elevated temperatures. One of our future works is to summarize more experimental data from other papers to obtain a more precisely model about stress-strain curves with temperature and rubber content.
- 2) Using TGA or EDS, XRD analysis to capture the variation on the C-S-H, CH and CaCO<sub>3</sub> under different high-temperature treatment.

## DATA AVAILABILITY STATEMENT

The original contributions presented in the study are included in the article/Supplementary Material, further inquiries can be directed to the corresponding authors.

## AUTHOR CONTRIBUTIONS

YT was responsible for experiment scheme design, test execution, and data analysis. WF was responsible for writing the original manuscript and theoretical guidance. ZC was responsible for experiment scheme guidance and manuscript revision. YN, MY, and JL were responsible for participating in test execution and data analysis.

## FUNDING

This research was funded by the National Natural Science Foundation of China (Grant No. 12032009,51578162).

ACI 216.1 (2007). *Code requirements for determining fire resistance of concrete and masonry construction assemblies*. Michigan, PA: American Concrete Institute.

Arulrajah, A., Disfani, M. M., Haghghi, H., Mohammadinia, A., and Horpibulsuk, S. (2015). Modulus of rupture evaluation of cement stabilized recycled glass/recycled concrete aggregate blends. *Construction Building Mater.* 84, 146–155. doi:10.1016/j.conbuildmat.2015.03.048

Asaro, L., Gratton, M., Seghar, S., and Ait Hocine, N. (2018). Recycling of rubber wastes by devulcanization. *Resour. Conservation Recycling* 133, 250–262. doi:10.1016/j.resconrec.2018.02.016

ASTM C39/C39M-20 (2020). *Standard test method for compressive strength of cylindrical concrete specimens*. West Conshohocken, PA: ASTM International.

ASTM C469/C469M-14 (2014). *Standard test method for static modulus of elasticity and Poisson's ratio of concrete in compression*. West Conshohocken, PA: ASTM International.

- ASTM C617/C617M-15 (2015). *Standard practice for capping cylindrical concrete specimens*. West Conshohocken, PA: ASTM International.
- Chen, A., Han, X., Chen, M., Wang, X., Wang, Z., and Guo, T. (2020). Mechanical and stress-strain behavior of basalt fiber reinforced rubberized recycled coarse aggregate concrete. *Construction Building Mater.* 260, 119888. doi:10.1016/j.conbuildmat.2020.119888
- Choe, G., Kim, G., Yoon, M., Hwang, E., Nam, J., and Guncunski, N. (2019). Effect of moisture migration and water vapor pressure build-up with the heating rate on concrete spalling type. *Cement Concrete Res.* 116, 1–10. doi:10.1016/j.cemconres.2018.10.021
- Choi, W.-C., and Yun, H.-D. (2012). Compressive behavior of reinforced concrete columns with recycled aggregate under uniaxial loading. *Eng. Structures* 41, 285–293. doi:10.1016/j.engstruct.2012.03.037
- Feng, W., Chen, B., Yang, F., Liu, F., Li, L., Jing, L., et al. (2021). Numerical study on blast responses of rubberized concrete slabs using the Karagozian and Case concrete model. *J. Building Eng.* 33, 101610. doi:10.1016/j.jobe.2020.101610
- Feng, W., Liu, F., Yang, F., Li, L., Jing, L., Chen, B., et al. (2019). Experimental study on the effect of strain rates on the dynamic flexural properties of rubber concrete. *Constr. Build. Mater.* 224, 408–419. doi:10.1016/j.conbuildmat.2019.07.084
- Feng, W., Liu, F., Yang, F., Li, L., and Jing, L. (2018). Experimental study on dynamic split tensile properties of rubber concrete. *Constr. Build. Mater.* 165, 675–687. doi:10.1016/j.conbuildmat.2018.01.073
- Ganjan, E., Khorami, M., and Maghsoudi, A. A. (2009). Scrap-tyre-rubber replacement for aggregate and filler in concrete. *Constr. Build. Mater.* 23, 1828–1836. doi:10.1016/j.conbuildmat.2008.09.020
- GB/T 50010-2010 (2015). *Code for the design of concrete structures*. Beijing, PA: Chinese standard.
- Graeff, A. G., Pilakoutas, K., Neocleous, K., and Peres, M. V. N. N. (2012). Fatigue resistance and cracking mechanism of concrete pavements reinforced with recycled steel fibres recovered from post-consumer tyres. *Eng. Structures* 45, 385–395. doi:10.1016/j.engstruct.2012.06.030
- Guo, Y., Xie, J., Zhao, J., and Zuo, K. (2019). Utilization of unprocessed steel slag as fine aggregate in normal- and high-strength concrete. *Constr. Build. Mater.* 204, 41–49. doi:10.1016/j.conbuildmat.2019.01.178
- Gupta, T., Chaudhary, S., and Sharma, R. K. (2014). Assessment of mechanical and durability properties of concrete containing waste rubber tire as fine aggregate. *Constr. Build. Mater.* 73, 562–574. doi:10.1016/j.conbuildmat.2014.09.102
- Gustavsson, L., Joelsson, A., and Sathre, R. (2010). Life cycle primary energy use and carbon emission of an eight-storey wood-framed apartment building. *Energy and Buildings* 42, 230–242. doi:10.1016/j.enbuild.2009.08.018
- Jiang, J. J., Ye, B., and Ma, X. M. (2014). The construction of Shenzhen's carbon emission trading scheme. *Energy Policy* 75, 17–21. doi:10.1016/j.enpol.2014.02.030
- Khouri, G. A. (2000). Effect of fire on concrete and concrete structures. *Prog. Struct. Engng Mater.* 2, 429–447. doi:10.1002/pse.51
- Koenders, E. A. B., Pepe, M., and Martinelli, E. (2014). Compressive strength and hydration processes of concrete with recycled aggregates. *Cement Concrete Res.* 56, 203–212. doi:10.1016/j.cemconres.2013.11.012
- Lee, G. C., and Choi, H. B. (2013). Study on interfacial transition zone properties of recycled aggregate by micro-hardness test. *Constr. Build. Mater.* 40, 455–460. doi:10.1016/j.conbuildmat.2012.09.114
- Li, L.-J., Tu, G.-R., Lan, C., and Liu, F. (2016). Mechanical characterization of waste-rubber-modified recycled-aggregate concrete. *J. Clean. Prod.* 124, 325–338. doi:10.1016/j.jclepro.2016.03.003
- Li, L.-J., Xie, W.-F., Liu, F., Guo, Y.-C., and Deng, J. (2011). Fire performance of high-strength concrete reinforced with recycled rubber particles. *Mag. Concrete Res.* 63, 187–195. doi:10.1680/mac.8.00140
- Li, L., and Chen, K. (2017). Quantitative assessment of carbon dioxide emissions in construction projects: a case study in Shenzhen. *J. Clean. Prod.* 141, 394–408. doi:10.1016/j.jclepro.2016.09.134
- Li, L., Ruan, S., and Zeng, L. (2014). Mechanical properties and constitutive equations of concrete containing a low volume of tire rubber particles. *Construction Building Mater.* 70, 291–308. doi:10.1016/j.conbuildmat.2014.07.105
- Li, M., Qian, C., and Sun, W. (2004). Mechanical properties of high-strength concrete after fire. *Cement Concrete Res.* 34, 1001–1005. doi:10.1016/j.cemconres.2003.11.007
- Liu, F., Meng, L.-y., Ning, G.-F., and Li, L.-J. (2015). Fatigue performance of rubber-modified recycled aggregate concrete (RRAC) for pavement. *Construction Building Mater.* 95, 207–217. doi:10.1016/j.conbuildmat.2015.07.042
- Liu, F., Zheng, W., Li, L., Feng, W., and Ning, G. (2013). Mechanical and fatigue performance of rubber concrete. *Construction Building Mater.* 47, 711–719. doi:10.1016/j.conbuildmat.2013.05.055
- Luo, Z., Yang, L., and Liu, J. (2016). Embodied carbon emissions of office building: a case study of China's 78 office buildings. *Building Environ.* 95, 365–371. doi:10.1016/j.buildenv.2015.09.018
- Meng, E., Yu, Y., Yuan, J., Qiao, K., and Su, Y. (2017). Triaxial compressive strength experiment study of recycled aggregate concrete after high temperatures. *Construction Building Mater.* 155, 542–549. doi:10.1016/j.conbuildmat.2017.08.101
- Mousa, M. I. (2017). Effect of elevated temperature on the properties of silica fume and recycled rubber-filled high strength concretes (RHSC). *HBRC J.* 13, 1–7. doi:10.1016/j.hbrj.2015.03.002
- Nagataki, S., Gokce, A., Saeki, T., and Hisada, M. (2004). Assessment of recycling process induced damage sensitivity of recycled concrete aggregates. *Cement Concrete Res.* 34, 965–971. doi:10.1016/j.cemconres.2003.11.008
- Pradhan, S., Kumar, S., and Barai, S. V. (2020). Multi-scale characterisation of recycled aggregate concrete and prediction of its performance. *Cement and Concrete Composites* 106, 103480. doi:10.1016/j.cemconcomp.2019.103480
- Reda Taha, M. M., El-Dieb, A. S., Abd El-Wahab, M. A., and Abdel-Hameed, M. E. (2008). Mechanical, fracture, and microstructural investigations of rubber concrete. *J. Mater. Civ. Eng.* 20, 640–649. doi:10.1061/(ASCE)0899-1561(2008)20:10(640)
- Saberian, M., Shi, L., Sidiq, A., Li, J., Setunge, S., and Li, C.-Q. (2019). Recycled concrete aggregate mixed with crumb rubber under elevated temperature. *Constr. Build. Mater.* 222, 119–129. doi:10.1016/j.conbuildmat.2019.06.133
- Sarhat, S. R., and Sherwood, E. G. (2013). Residual mechanical response of recycled aggregate concrete after exposure to elevated temperatures. *J. Mater. Civ. Eng.* 25, 1721–1730. doi:10.1061/(ASCE)MT.1943-5533.0000719
- Tam, V. W. Y., Gao, X. F., and Tam, C. M. (2005). Carbonation around near aggregate regions of old hardened concrete cement paste. *Cement Concrete Res.* 35, 1180–1186. doi:10.1016/j.cemconres.2004.07.042
- Tang, Y.-C., Li, L.-J., Feng, W.-X., Liu, F., and Zhu, M. (2018). Study of seismic behavior of recycled aggregate concrete-filled steel tubular columns. *J. Constructional Steel Res.* 148, 1–15. doi:10.1016/j.jcsr.2018.04.031
- Tang, Y., Fang, S., Chen, J., Ma, L., Li, L., and Wu, X. (2020). Axial compression behavior of recycled-aggregate-concrete-filled GFRP-steel composite tube columns. *Eng. Structures* 216, 110676. doi:10.1016/j.engstruct.2020.110676
- Tang, Y., Li, L., Wang, C., Chen, M., Feng, W., Zou, X., et al. (2019). Real-time detection of surface deformation and strain in recycled aggregate concrete-filled steel tubular columns via four-ocular vision. *Robotics and Computer-Integrated Manufacturing* 59, 36–46. doi:10.1016/j.rcim.2019.03.001
- Xiao, J., Fan, Y., and Tawana, M. M. (2013). Residual compressive and flexural strength of a recycled aggregate concrete following elevated temperatures. *Struct. Concrete* 14, 168–175. doi:10.1002/suco.201200037
- Xiao, J., Wang, C., Ding, T., and Akbarnezhad, A. (2018). A recycled aggregate concrete high-rise building: structural performance and embodied carbon footprint. *J. Clean. Prod.* 199, 868–881. doi:10.1016/j.jclepro.2018.07.210
- Xie, J., Fang, C., Lu, Z., Li, Z., and Li, L. (2018). Effects of the addition of silica fume and rubber particles on the compressive behaviour of recycled aggregate concrete with steel fibres. *J. Clean. Prod.* 197, 656–667. doi:10.1016/j.jclepro.2018.06.237
- Xie, J., Zheng, Y., Guo, Y., Ou, R., Xie, Z., and Huang, L. (2019). Effects of crumb rubber aggregate on the static and fatigue performance of reinforced concrete slabs. *Compos. Structures* 228, 111371. doi:10.1016/j.compstruct.2019.111371
- Xiong, Z., Cai, Q., Liu, F., Li, L., and Long, Y. (2020). Dynamic performance of RAC-filled double-skin tubular columns subjected to cyclic axial compression. *Construction Building Mater.* 248, 118665. doi:10.1016/j.conbuildmat.2020.118665
- Xuan, D., Zhan, B., and Poon, C. S. (2017). Thermal and residual mechanical profile of recycled aggregate concrete prepared with carbonated concrete aggregates after exposure to elevated temperatures. *Fire Mater.* 42, 134–142. doi:10.1002/fam.2465

**Conflict of Interest:** The authors declare that the research was conducted in the absence of any commercial or financial relationships that could be construed as a potential conflict of interest.

Copyright © 2021 Tang, Feng, Chen, Nong, Yao and Liu. This is an open-access article distributed under the terms of the Creative Commons Attribution License (CC BY). The use, distribution or reproduction in other forums is permitted, provided the original author(s) and the copyright owner(s) are credited and that the original publication in this journal is cited, in accordance with accepted academic practice. No use, distribution or reproduction is permitted which does not comply with these terms.